Clumped-isotope constraint on upper-tropospheric cooling during the Last Glacial Maximum

Asmita Banerjee[1,*], Laurence Y. Yeung[1,2,*], Lee T. Murray[3], Xin Tie[3], Jessica E. Tierney[4], and Allegra N. Legrande[5]

[1]Department of Earth, Environmental and Planetary Sciences, Rice University, Houston, TX, USA

[2]Department of Chemistry, Rice University, Houston, TX, USA

[3]Department of Earth and Environmental Sciences, University of Rochester, Rochester, NY, USA

[4]Department of Geosciences, University of Arizona, Tucson, AZ, USA

[5]NASA Goddard Institute for Space Studies and Center for Climate Systems Research, Columbia University, New York, USA

Corresponding author: Asmita Banerjee (Asmita.Banerjee@rice.edu) , Laurence Y. Yeung (lyeung@rice.edu)

Key Points:

- Measurements of O_2 clumped isotopes in polar ice cores are compared to predictions from 3-dimensional chemical transport modeling
- Measured and modeled change in O_2 clumped isotope values between the Last Glacial Maximum and Preindustrial agree within uncertainty
- Clumped-isotope results imply a minor lapse-rate steepening at the Last Glacial Maximum relative to the Preindustrial

Abstract

Ice cores and other paleotemperature proxies, together with general circulation models, have provided information on past surface temperatures and the atmosphere's composition in different climates. Little is known, however, about past temperatures at high altitudes, which play a crucial role in Earth's radiative energy budget. Paleoclimate records at high-altitude sites are sparse, and the few that are available show poor agreement with climate model predictions. These disagreements could be due to insufficient spatial coverage, spatiotemporal biases, or model physics; new records that can mitigate or avoid these uncertainties are needed. Here, we constrain the change in upper-tropospheric temperature at the global scale during the Last Glacial Maximum (LGM) using the clumped-isotope composition of molecular oxygen trapped in polar ice cores. Aided by global three-dimensional chemical transport modeling, we exploit the intrinsic temperature sensitivity of the clumped-isotope composition of atmospheric oxygen to infer that the upper troposphere (5 – 15 km altitude, effective mean 10 – 11 km) was 4 – 10°C cooler during the LGM than during the late preindustrial Holocene. These results support a minor or negligible steepening of atmospheric lapse rates during the LGM, which is consistent with a range of climate model simulations. Proxy-model disagreements with other high-altitude records may stem from inaccuracies in regional hydroclimate simulation, possibly related to land-atmosphere feedbacks.

Plain Language Summary

Atmospheric temperatures at high altitudes determine the fate of montane glaciers and the energy balance of the planet. They change with Earth's climate, but our knowledge of this relationship is poor: the few available temperature records for high-altitude cooling at the most recent ice age, which are limited to the tropics, disagree with model predictions for unknown reasons. Here we report a global-scale constraint for high-altitude temperature, applied to the last ice age, which yields results consistent with global climate model predictions. This new proxy—based on the isotopic variants of molecular oxygen trapped in polar ice cores—can be applied deeper in the past to understand the relationship between surface and high-altitude temperatures in different climates.

1 Introduction

Atmospheric lapse rates affect the emission of longwave radiation to space and thus the climate system's response to changes in greenhouse gas concentrations (Bony et al., 2006; Soden & Held, 2006) Accurately predicting how they and other atmospheric properties change when subject to different climate forcing, however, remains a challenge (Bony et al., 2006, 2015; Shepherd, 2014; Sherwood et al., 2014). Simulated lapse-rate responses to climate forcing differ substantially among models and they are, on average, a factor of two smaller than what proxy-based reconstructions imply for the most recent glacial period in the tropics (Farrera et al., 1999; Porter, 2000; Kageyama et al., 2005; Soden & Held, 2006; Loomis et al., 2017). However, the high-altitude paleoclimate record is sparse and biased toward terrestrial signals; it yields few constraints on how large-scale atmospheric temperature structure changes with surface climate. A global-scale high-altitude paleotemperature proxy, unaffected by location-specific climatology, could benchmark climate model performance at high altitudes for past climates and diagnose any shortcomings in model physics.

The Last Glacial Maximum (LGM, 21-18 ka) has been used extensively as a reference climate state for paleoclimate modeling and to constrain climate sensitivity due to its relatively recent occurrence, well-preserved proxy records, and radically different climate forcings (Braconnot et al., 2012; Otto-Bliesner et al., 2006; Schmittner et al., 2011; Kageyama et al., 2017; Tierney et al., 2020; Kageyama et al., 2021). Reduced greenhouse-gas concentrations and the presence of large ice sheets (Anklin et al., 1997; Monnin et al., 2001; Valdes, 2005; Spahni et al., 2005; Loulergue et al., 2008; Parrenin et al., 2013) led to a global-scale cooling of surface air temperatures (SATs). Estimates using model-data syntheses suggest that global-mean SATs were between 4°C and 6°C cooler than the late preindustrial Holocene (Annan & Hargreaves, 2013; Tierney et al., 2020), while noble gas-based low- and mid-latitude temperature estimates suggest 6°C of cooling on land (Seltzer et al., 2021). High-altitude cooling during the LGM, however, is less well known. For example, many paleotemperature records from polar ice cores reflect climate at high elevations, but weak constraints on ice-sheet elevation histories complicate their utility as high-altitude records. Tropical ice cores, glacier equilibrium line altitudes, pollen assemblages and organic geochemical proxies preserved in high-altitude lake sediments have provided the primary paleoclimatic constraints (Thompson et al., 1995, 1998; Farrera et al., 1999; Porter, 2000; Thompson, 2000; Thompson et al., 2003; Stansell et al., 2007). Proxy based estimates typically report a ~1°C/km steepened lapse rate in the tropics with poorly characterized regional-scale variability (Farrera et al., 1999; Loomis et al., 2017). General circulation models, however, consistently simulate a weaker lapse rate steepening of 0.2 – 0.6°C/km in the tropics (Kageyama et al., 2005; Loomis et al., 2017) and a much weakened lapse rate over the Northern Hemisphere polar ice sheets (Abe-Ouchi et al., 2007). This proxy-model disparity prompts questions as to whether models are accurately capturing global-scale behavior at high altitudes, or whether disagreements arise from shortcomings in regional-scale climate prediction.

Clumped isotopes of oxygen (i.e., the proportional abundance of $^{18}O^{18}O$ in O_2, reported as a Δ_{36} value; see Methods) can provide novel constraints on past global-mean free-tropospheric temperatures (Yeung et al., 2016, 2021). In the atmosphere, $O(^3P) + O_2$ isotope-exchange reactions enrich $^{18}O^{18}O$ in O_2 relative to what chance alone would dictate, elevating its Δ_{36} value (Wang et al., 2004; Yeung et al., 2012, 2014). These enrichments increase as temperatures decrease: at photochemical steady state, the Δ_{36} temperature sensitivity can be as high as +0.025‰ per

°C cooling depending on local temperature and pressure. Moreover, the mean altitude where oxygen isotope-exchange reactions occur is 10 ± 5 km, with a mean altitude in the tropics that is ~2 km higher than in the extratropics. Thus, the majority of tropospheric isotope-exchange reactions occur in the upper troposphere, and the Δ_{36} value of tropospheric O_2 should vary inversely with the temperatures there; efficient stirring of the troposphere on annual timescales largely removes local-scale effects (Yeung et al., 2021). However, the tropospheric Δ_{36} value is also sensitive to the tropospheric O_3 burden—which controls mean tropospheric O(^3P) concentrations—and inputs of high-Δ_{36} stratospheric O_2 on sub-decadal timescales. For global temperature changes exceeding several degrees Celsius, upper-tropospheric temperature changes may dominate over these other terms in the global Δ_{36} budget (Yeung et al., 2016). Consequently, the Δ_{36} value of O_2 is expected to vary with global climate. Here, we report new clumped-isotope measurements of O_2 trapped in polar ice cores and argue that they constrain the upper-tropospheric temperature change between the LGM and the late preindustrial Holocene (PI). We use the Ice Age Chemistry and Proxies (ICECAP) modeling framework (Murray et al., 2014; Murray et al., 2021) to estimate tropospheric O_3 changes and infer climate-driven changes in atmospheric temperature structure.

2 Materials and Methods

2.1 O_2 clumped-isotope measurements. Ice core samples drilled from the Greenland Ice Sheet Project (GISP2-D core) and West Antarctic Ice Sheet Divide Ice Core (WDC06A core) were used for this study. The depths for the WDC06A and GISP2-D ice cores span 2450 – 2556 m and 1900 – 1962 m respectively, corresponding to gas ages of 18 – 21ka (Rasmussen et al., 2014; Seierstad et al., 2014; Buizert et al., 2015; Sigl et al., 2016). For every analysis, 90 – 100g of ice core sample was used, with an average O_2 yield of ~70 mbar using previously described methods (Severinghaus et al., 2003; Yeung et al., 2019). Collected samples were purified cryogenically using a gas chromatograph (GC) to remove nitrogen, argon and other trace gases. Subsequently, the O_2 isotopologue ratios were measured using a high-resolution Nu Instruments *Perspective IS* isotope ratio mass spectrometer (Yeung et al., 2016). Clumped isotope compositions of O_2 are described by a Δ_{36} value, reported against the stochastic (random) distribution of isotopes within that sample:

$$\Delta_{36} = \left(\frac{^{36}R_{measured}}{^{36}R_{stochastic}} - 1 \right) \quad (1)$$

where

$$^{36}R_{stochastic} = \frac{[^{18}O][^{18}O]}{[^{16}O][^{16}O]} = (^{18}R)^2 \quad (2)$$

Reported Δ_{36} values are calibrated against low-pressure (<2 mbar) photochemical standards generated at a range of temperatures (-63°C to 25°C) and also high temperature standards (800°C) generated by thermal decomposition of barium peroxide (Yeung et al., 2014). We note that at low pressures, the $^{18}O^{18}O$ enrichment resembles isotopic equilibrium, whereas at higher pressures, the $^{18}O^{18}O$ enrichment is smaller due to a titration of heavy O_2 isotopologues into O_3 (Yeung et al., 2021). This pressure effect influences the computation of the atmospheric Δ_{36} values in the

model described below, but does not impact the comparison of Δ_{36} values reported herein with prior published values, as the calibration methods are identical.

2.2 Data correction and rejection criteria. We measured a total of 102 ice-core samples (n = 53 for GISP, n = 49 for WDC) but exclude 27 of those samples from our results. The reported dataset has a spread greater than the reported difference between the LGM-PI and LGM-PD. The spread in the reported data implicitly includes both instrumental uncertainty (i.e., shot noise + Johnson noise, leading to a combined uncertainty of ±0.03‰) and sample-processing artifacts. Our data filtering method to account for sample processing-related uncertainty is primarily based on the raw $\delta^{18}O$ values of O_2 measured previously (Severinghaus et al., 2009; Severinghaus, 2015) and is explained in Text S1. Irrespective of the data rejection criteria applied, however, both unfiltered (n = 102) and filtered (n = 75) datasets have the same mean Δ_{36} value and confidence intervals (Figure S1). Consequently, the results do not depend critically on the data rejection criteria used.

2**.3 Atmospheric chemistry modeling.** Atmospheric chemistry simulations for online Δ_{36} calculations were performed using GEOS-Chem (version 12.9.0; http://www.geos-chem.org), a three-dimensional global chemical transport model with the unified chemical mechanism [UCX; (Eastham et al., 2014)] driven by the meteorology of the Goddard Institute of Space Science E2.1 model archived at 2° latitude by 2.5° longitude spatial and 3-h (3-D) and hourly (2-D) temporal resolution, which contains 40 vertical layers extending from the surface to about 60 km (about 28 in the tropical troposphere) [GISS-E2.1; (Rind et al., 1988; Schmidt et al., 2006; Murray et al., 2014; Kelley et al., 2020; Murray et al., 2021)]. The simulations reported here degrade the GISS-E2.1 spatial resolution to 4° × 5° (latitude × longitude) for computational expediency.

2.3.1 Updates to halogen chemistry and its effect on ozone concentrations. An updated set of heterogeneous halogen mechanisms were included in ICECAP for an updated tropospheric bromine chemistry and an extension of stratospheric chlorine mechanism to the troposphere (Eastham et al., 2014; Schmidt et al., 2016). Iodine and a more comprehensive chlorine-bromine-iodine mechanism were then applied (Sherwen et al., 2016) as well as the oxidation of dissolved SO_2 by HOBr (Chen et al., 2017). Recent updates to halogen chemistry in ICECAP include chlorine mobilization of sea salt aerosol from HCl acid displacement and other heterogeneous processes, and improved aerosol and cloud chemistry (Wang et al., 2019, 2021).

We note that tropospheric ozone concentrations can be affected by halogen species in the troposphere through reactions with NO_x (NO_2 + NO) and its reservoir species. For example, $ClNO_2$ formed through Cl^- + N_2O_5 during the night can be photolyzed during the daytime to produce NO_2 to increase the ozone concentration (Osthoff et al., 2008; Roberts et al., 2008). Fast cycling between halogen radicals and their reservoir species enhances the conversion from NO_x to HNO_3 which leads to catalytic ozone loss (von Glasow et al., 2004; Yang et al., 2005; Sherwen et al., 2016). Furthermore, other major oxidants like dimethylsulfide and volatile organic compounds that influence ozone concentration can be lost through reaction with Cl, Br and I atoms (Atkinson, 1997; Saiz-Lopez & Glasow, 2012; Horowitz et al., 2017).

2.3.2 Meteorologies used in GEOS-Chem. The climate in GISS-E2.1 used in this study is run in atmosphere-only mode and forced by ice core estimates of greenhouse gas concentrations, sea ice, topography, sea surface temperature and orbital parameters as described previously (Murray et al., 2014). The LPJ-LMfire model is

used to represent an upper limit on the fire activity of the past ("high-fire" scenario) and yields fire emissions 3-4 times higher than those for the present day (Pfeiffer et al., 2013; Murray et al., 2014; Kaplan et al., 2016). The lower limit on fire activity ("low-fire" scenario) is based on the charcoal accumulation rates from the Global Charcoal Database and has been described in Murray et al., (2014).

In addition to using physically consistent LGM sea-surface temperature (SST) climatologies generated by GISS-E2.1—from the fully-coupled online ocean of the Paleoclimate Model Intercomparison Project-3 (PMIP3) experiment (Braconnot et al., 2012)—we also performed an alternative simulation in atmosphere-only mode, using monthly SST climatologies derived from an updated version of the LGM data assimilation product of Tierney et al., (2020). The original LGM data assimilation product in Tierney et al., (2020) computed only annual mean quantities of SST, so for the purposes of this manuscript we re-ran the data assimilation to output monthly quantities. The underlying proxy data, forward models, and data assimilation settings were identical to those used in Tierney et al., (2020); however, a wider range of model priors were used for both the LGM and Late Holocene (LH) assimilations following Osman et al., (2021). The model priors for the LGM timeslice included the three experiments used in Tierney et al., (2020) (iCESM1.2-21ka, iCESM1.3-21ka, iCESM-18ka) plus an additional iCESM1.2-16ka experiment. The model priors for the LH timeslice include the three experiments used in Tierney et al., (2020) (iCESM1.2-PI, iCESM1.3-PI, iCESM-3ka) plus an iCESM1.2-PI experiment with prognostic phenology and the iCESM1.2 Last Millennium Ensemble with prognostic phenology. The posterior LGM data assimilation has a global mean surface temperature (GMST) of 7.4˚C, which is nearly identical to the GMST of the original LGM data assimilation in Tierney et al., (2020) (7.5˚C). The posterior LH data assimilation, however, has a GMST of 12.8˚C, which is 0.8˚C colder than in Tierney et al., (2020) (13.6˚C). The colder LH posterior is a consequence of including priors with prognostic phenology in the land model (which have a colder GMST), rather than only including simulations with a prescribed phenology, as was done in Tierney et al., (2020). The LH proxies apparently favor a colder solution, a finding supported by the rank histogram analysis in Extended Data Figure 2 of Tierney et al., (2020), which shows that more proxies lie below the prior (i.e. are colder) than above it. With a cooler LH GMST, the magnitude of cooling in this updated version of the LGM data assimilation is -5.4˚C. This updated version of the LGM data assimilation, *lgmDA version 2.0* (Tierney & Osman, 2021), is publicly available at https://doi.org/10.5281/zenodo.5171432.

2.3.3 Online Δ_{36} calculation schemes. Similar to previous work (Yeung et al., 2021), two online Δ_{36} calculation schemes (pressure-independent and pressure-dependent) were implemented in GEOS-Chem to assess the sensitivity of the model results to Δ_{36} parameterization. In the pressure-independent scheme, atmospheric Δ_{36} values trend toward isotopic equilibrium according to the local kinetics of oxygen isotope exchange. In the pressure-dependent scheme, Δ_{36} approaches an isotopic steady state governed by local temperature and pressure, which varies according to the relative rates of isotope exchange and O_3 isotopologue formation. In both schemes, atomic oxygen ($[O^3(P)]$) concentration and local temperature are the primary drivers of the instantaneous rates of isotope exchange. The pressure-dependent scheme reproduces modern observations quantitatively across latitudes, years, and seasons (Yeung et al., 2021), so those results are reported in the main text. The results of the pressure-independent calculation of Δ_{36} values are shown in Tables S1 and S2; the simulated Δ_{36} differences between the time periods of interest are

nearly identical, despite the absolute magnitude of Δ_{36} values being different. The choice of Δ_{36} calculation scheme does not affect the interpretations.

2.3.4 Estimating the spatial distribution and mean effective isotope re-ordering altitude using outputs from GEOS-Chem simulations. The isotope exchange rate in the troposphere, E_{trop}, can be determined using the following equation described previously (Yeung et al., 2021):

$$E_{trop} = \frac{\Sigma_{trop\ grid\ boxes} k_{exch}(T)[\mathrm{O}(^3P)][\mathrm{O_2}] m_{box} \rho_{box}^n}{\Sigma_{trop\ grid\ boxes} m_{box} \rho_{box}^n} \times V_{trop} \quad (3)$$

where $k_{exch}(T)[\mathrm{O}(^3P)][\mathrm{O_2}]$ is the local rate of isotope exchange in units of concentration per unit time; m_{box} is the mass of air used to normalize for the variable size of grid boxes, and V_{trop} is the volume of the troposphere. ρ_{box} is the air density of each grid box. The exponent n is used to acknowledge factors that affect the progression of Δ_{36} toward steady state; it reflects the balance between the residence time of air parcels within grid boxes (which drives $n \rightarrow 1$) and the efficiency with which air parcels are isotopically reordered within each box (which drives $n \rightarrow -1$). In general, this balance varies with climate and atmospheric chemistry, and ranges from −0.6 to −0.7 for the LGM simulations reported here.

3 Ice core measurements and atmospheric chemistry modeling results

3.1 Ice-core measurements. LGM-aged oxygen from the West Antarctic Ice Sheet Divide (WDC06A core) (Buizert et al., 2015) and Greenland Ice Sheet Drilling Project (GISP2-D core) (Seierstad et al., 2014) ice cores has a mean Δ_{36} value of 2.10 ± 0.06‰ (1σ, n = 32) and 2.09 ± 0.04‰ (1σ, n = 43), respectively (Figure 1). While the time-dependent variability of these values exceeds that expected from instrumental uncertainty and thus may contain additional paleoatmospheric information (see Text S1), we focus here on the longer-term mean LGM state. Bootstrap resampling of the LGM data from both cores yields a mean LGM tropospheric Δ_{36} value of 2.10 ± 0.01 (95% confidence interval, CI) with no statistically significant difference between the two cores (p = 0.31) (See Section 2.2, Figure S1). This mean LGM Δ_{36} value is higher than PI and present-day (PD) values by 0.06 ± 0.01‰ and 0.09 ± 0.02‰, respectively (95% CI; Figure 1) (Yeung et al., 2019).

If temperature were the only control on tropospheric Δ_{36} values, the shift in mean value would imply that upper-tropospheric temperatures during the LGM were 5 ± 1°C cooler than the PI, on average, because the sensitivity of steady-state Δ_{36} values to temperature is ~0.013 ‰/°C in the upper troposphere (i.e., at pressures ranging from 250 – 450 mbar) (Figure 2). However, changes in atmospheric O_3, its spatial distribution, and other physical processes may alter this estimate by changing the relative importance of tropospheric and stratospheric influences on the tropospheric Δ_{36} value.

3.2 Atmospheric modeling results. To constrain potential changes in tropospheric O_3 since the LGM, we simulated the atmospheric chemistry of the LGM, PI, and PD using the ICECAP modeling framework. LGM model results are referred to as LGM-GISS and LGM-DA, corresponding to the meteorologies arising from fully coupled runs of GISS-E2.1 and those from atmosphere-only runs of GISS-E2.1 with prescribed monthly SSTs, respectively.

Importantly, the two meteorologies differ in their LGM cooling: the mean SAT cooling is 3.9°C (LGM-GISS) and 4.9°C (LGM-DA) compared to the PI, with a mean SAT cooling of 2.5°C and 3.7°C in the tropics (30°N – 30°S), respectively (Figure S2). The mean upper-tropospheric cooling between 10 km and 11 km altitude is 4.0-4.3°C and 6.0-6.5°C in the tropics, respectively (Figure 3).

The atmospheric chemistry results are shown in Table 1. From the LGM to the PI, the modeled global tropospheric O_3 burden increases by 5-8% and 12-18% for the high- and low-fire scenarios, respectively (Table S2). The sign of the modeled O_3 change is consistent with earlier studies; however, the magnitude is generally smaller than that found in all previous simulations (i.e., 17 – 30%) (Thompson et al., 1993; Martinerie et al., 1995; Valdes, 2005; Kaplan et al., 2006; Murray et al., 2014) except the most recent estimates of tropospheric O_3 at the LGM (Wang et al., 2020). The reduced magnitude of the tropospheric O_3 change in the simulations reported here is attributed largely to the incorporation of more comprehensive halogen chemistry in GEOS-Chem, the atmospheric chemistry module of ICECAP (see Methods) (Sherwen et al., 2016; Wang et al., 2019).

Analysis of the modeled spatial patterns of $O(^3P) + O_2$ isotope exchange reveals that the effective mean altitude recorded by the Δ_{36} tracer is ~11km in all scenarios reported here (Table 1, Figure S3), with a slight bias toward the tropical upper troposphere (Figure S3). This effective mean altitude for the present day is 1km higher than previously found using the Modern Era Retrospective Reanalysis-2 (MERRA2) meteorology and GEOS-Chem (Yeung et al., 2021). Similar to the calculation of Δ_{36} values, this slight difference in spatial patterns of isotope exchange between GISS-E2.1 and MERRA2 meteorologies is mitigated when comparing within a model framework due to cancellation of errors. The latitudinal pattern for all scenarios (roughly 49% tropical, 43% midlatitude, 8% polar) largely resembles that of Earth's surface area (47% tropical, 40% midlatitude, and 13% polar).

The simulated global-mean surface Δ_{36} values (i.e., $\Delta_{36,trop}$; Table 1) are slightly higher than the measurements, but the modeled changes in surface Δ_{36} values are similar for both LGM meteorologies (Figure 4). Specifically, the modeled LGM-to-PI change ranges from –0.05‰ and –0.08‰, while the modeled PI-to-PD change is –0.04‰ and –0.06‰ for high- and low-fire scenarios, respectively (Table S2 and Figure 4). Modeled variations in global-mean surface Δ_{36} values benefit from a cancellation of systematic errors (Yeung et al., 2021), resulting in higher expected accuracy for changes in Δ_{36} values between LGM, PI, and PD scenarios. The high-fire emissions scenarios yield modeled Δ_{36} changes in better agreement with those measured in ice cores; low-fire model scenarios yield larger Δ_{36} changes, with pronounced disagreements with observations when comparing changes against the PD. Moreover, the LGM-DA simulations show better agreement with observations than LGM-GISS simulations when compared to the PI; the former have tropospheric temperatures that are ~1°C cooler and Δ_{36} values that are ~0.01‰ higher. The modeled LGM-to-PI changes in Δ_{36} value are, in all cases, associated with a colder free troposphere, a smaller tropospheric O_3 burden during the LGM, and changes in stratosphere-troposphere exchange.

4 Discussion

4.1 Tropospheric Δ_{36} values are sensitive to global climate and atmospheric chemistry. To attribute changes in the tropospheric Δ_{36} value to upper-tropospheric temperature, tropospheric O_3, and stratosphere-troposphere exchange, we use a two-box model approach described by the equation (Yeung et al., 2021):

$$\Delta_{36,\mathrm{trop}} \approx \left(\frac{E_{trop}}{F_{ST}+E_{trop}}\right)\Delta_{36,\mathrm{t}} + \left(\frac{F_{ST}}{F_{ST}+E_{trop}}\right)\Delta_{36,\mathrm{strat}} \quad (4)$$

Here, $\Delta_{36,\mathrm{trop}}$ is equivalent to the global-mean surface Δ_{36} value, F_{ST} (mol O_2 yr^{-1}) is the stratosphere-to-troposphere transport (STT) flux of O_2, E_{trop} (mol O_2 yr^{-1}) is the effective rate of $O(^3P)$ + O_2 isotope exchange in the troposphere, $\Delta_{36,\mathrm{t}}$ is the Δ_{36} value for isotope exchange occurring only in the troposphere, and $\Delta_{36,\mathrm{strat}}$ is the Δ_{36} value for isotope exchange occurring only in the stratosphere. These last two terms represent endmember Δ_{36} values. The relative tropospheric and stratospheric contributions to the $\Delta_{36,\mathrm{trop}}$ value are determined by the terms attendant to the $\Delta_{36,\mathrm{t}}$ and $\Delta_{36,\mathrm{strat}}$ values, respectively, in eq. 4. In practice, F_{ST} is inferred from model outputs corresponding to each of the other four quantities (see Methods). Examining the effects of changing these quantities individually allows one to attribute the importance of each variable ($\Delta_{36,\mathrm{t}}$, $\Delta_{36,\mathrm{strat}}$, or E_{trop} and F_{ST} together) to the overall change in $\Delta_{36,\mathrm{trop}}$ value between scenarios.

The inferred values of each variable in eq. 4 can be found in Table 1. We find that the $\Delta_{36,\mathrm{t}}$ decrease accounts for roughly half (46% – 65%) of the LGM-to-PI change in $\Delta_{36,\mathrm{trop}}$ value in the model, with high-fire scenarios on the lower end of the range. The changing balance of E_{trop} and F_{ST} accounts for about one-third (26% – 45%) of the change in $\Delta_{36,\mathrm{trop}}$ value, with high-fire scenarios constituting the upper part of the range. The $\Delta_{36,\mathrm{strat}}$ increase, which arises from subtle changes in temperature and O_3 photochemistry near the tropopause, accounts for the remainder (6% – 13%), with high-fire scenarios constituting the upper part of the range. Therefore, while the cooling in the LGM simulations is consistent with the cooling implied by a simple interpretation of the observed tropospheric Δ_{36} change, the observed tropospheric Δ_{36} change likely has more complex climate-dependent origins.

4.2 Evaluating the effects of climate-dependent changes to the Δ_{36} proxy budget. Below, we discuss the potential climate-dependent changes to tropospheric O_3 chemistry, STT fluxes, the stratospheric $\Delta_{36,\mathrm{strat}}$ signature, as well as the effective mean altitude of the Δ_{36} proxy, and their effects on a Δ_{36}-based upper-tropospheric cooling estimate. These estimated changes to the tropospheric Δ_{36} budget will then be used to estimate a conservative range for upper tropospheric cooling during the LGM using an energy balance approach.

4.2.1 Tropospheric O_3 burden. While no direct measurements of LGM tropospheric O_3 exist, lower atmospheric mixing ratios of CH_4 suggest that the LGM tropospheric O_3 burden was lower than during the PI (Murray et al., 2014). Indeed, a lower tropospheric O_3 burden is a robust feature of all LGM chemistry simulations to date (Thompson et al., 1993; Martinerie et al., 1995; Valdes, 2005; Kaplan et al., 2006; Murray et al., 2014; Wang et al., 2020), including this study and a model that is consistent with ice-core constraints offered by the ^{17}O content of sulfate and nitrate (Alexander et al., 2002; Geng et al., 2017). The lower tropospheric O_3 burden at the LGM leads to a reduction in E_{trop} (Table 1), which results in a cold bias in the Δ_{36} proxy, i.e., a higher tropospheric Δ_{36} value compared to that driven by cooling alone.

298 **4.2.2 Stratosphere-to-troposphere transport**. The climate sensitivity of the STT flux of O_2 (i.e., F_{ST})—and
299 thus its contribution to tropospheric Δ_{36}—remains uncertain. General circulation models show that the Brewer-Dobson
300 Circulation (BDC), which governs the STT flux, is sensitive to climate (Holton et al., 1995; Rind et al., 2001, 2009;
301 Fu et al., 2015; Geng et al., 2017; Fu et al., 2020): some studies infer a strengthened BDC (Rind et al., 2001, 2009;
302 Geng et al., 2017) while others infer a weakened BDC during the LGM (Fu et al., 2020; Wang et al., 2020). Estimates
303 of the LGM-to-PI change in STT flux thus range from +20% to –17%. Changes in the STT flux of O_3 on this order
304 are expected to have negligible effects (<1%) on the tropospheric O_3 burden (Neu et al., 2014)
305 Based on the analysis of model derived outputs, the strengthened STT flux combined with a lower E_{trop} value
306 in our LGM simulations contributes up to 0.026‰ (i.e., a 2°C cold bias) to the LGM-to-PI change in $\Delta_{36,trop}$ value. If
307 the BDC instead weakened by 10 – 20% during the LGM (Fu et al., 2020; Wang et al., 2020), its change would mirror
308 that expected for E_{trop}, minimizing the proportional change in the flux terms of the tropospheric $\Delta_{36,trop}$ budget [i.e.,
309 $E_{trop}/(E_{trop} + F_{ST})$ and $F_{ST}/(E_{trop} + F_{ST})$ in eq. 4]. This latter scenario would result in $\Delta_{36,t}$ (i.e., mostly the tropospheric
310 temperature change) driving the change in $\Delta_{36,trop}$ value. Therefore, given high confidence for a reduction in E_{trop} at
311 the LGM, the uncertainty in the STT flux of O_2 would likely yield a combined ($E_{trop} + F_{ST}$) cold bias in the Δ_{36} proxy
312 temperature of 0 – 2°C.
313 **4.2.3. Stratospheric Δ_{36} signature.** The change in the stratospheric Δ_{36} endmember signature ($\Delta_{36,strat}$)
314 between the LGM and PI, arising from changes in stratospheric temperatures and O_3 concentrations, has a minor effect
315 on the $\Delta_{36,trop}$ budget. The modeled LGM-to-PI change of –0.04‰ in the $\Delta_{36,strat}$ value translates to a <0.01‰ effect on
316 the $\Delta_{36,trop}$ value. Its uncertainty, while difficult to ascertain *a priori*, is likely negligible compared to the uncertainties
317 in the tropospheric O_3 burden and STT flux of O_2.
318 **4.2.4. Effective mean altitude of isotope exchange.** The LGM and PI temperatures need to be compared at
319 equivalent altitudes. Sea-level change, for example, lowers the sea-surface reference point at the LGM by ~130 m. In
320 addition, the reduction in atmospheric water vapor during the LGM is expected to lower the height of the Hadley cell
321 and tropopause (Schneider et al., 2010; Murray et al., 2014). These changes lower the mean altitude at which
322 tropospheric oxygen-isotope exchange reactions occur, and thus result in a warm bias for the Δ_{36} proxy temperature
323 at the LGM. The minimum warm bias, from the sea-level change alone, can be estimated to be ~1°C using lapse rates
324 ranging from 6.5°C/km (i.e., the modern mean) to 9.8°C/km (i.e., the dry adiabat). However, the effects of circulation
325 changes—which would redistribute tropospheric O_3 to lower altitudes, on average, during the LGM—are not as
326 straightforwardly estimated.
327 Some constraints on the these effects can be obtained using an energy balance approach. We will first recast
328 the change in effective altitude for isotope reordering ($\Delta Z_{eff} < 0$ for lowering) as the sum of contributions from changes
329 in spatial distribution of tropospheric ozone (ΔZ_{O3}), tropopause height (ΔZ_{TP}, which is linked to the lapse rate; see
330 below), and sea level (ΔZ_{SL}), i.e.,

331 $$\Delta Z_{eff} = \Delta Z_{O3} + \Delta Z_{TP} + \Delta Z_{SL} \quad (5)$$

332 Comparison of the high-fire and low-fire scenarios in our atmospheric chemistry simulations reveals a
333 consistent increase in the effective reordering altitude of 22 – 23 m for every 1% decrease in the tropospheric O_3
334 burden (Table 2). This relationship for ΔZ_{O3} is that associated with biomass burning emissions, the largest uncertainty

in the past tropospheric O_3 budget. The LGM-DA simulation, which has a climate closer to that of the LGM data assimilation, yields ΔZ_{O3} = 0.2 km and 0.4 km for the high- and low-fire scenarios.

The value of ΔZ_{TP} between the LGM and PI is determined by radiative and dynamical constraints, which yield a quantitative relationship between Z_{TP}, surface temperature (T_s), the tropospheric longwave emission height (Z_e), and the lapse rate ($\Gamma > 0$, nominally 6.5°C/km) (Schneider et al., 2010; Thuburn & Craig, 2000):

$$Z_{TP} \approx (1 - c)\frac{T_s}{\Gamma} + cZ_e \quad (6)$$

Here, $c = 2^{-1/4} \approx 0.84$. If T_s is known, one can determine Z_e by solving the one-dimensional energy balance for the atmospheric emission temperature (T_e) and then using Γ to determine Z_e:

$$\sigma T_e^4 = S(1 - \alpha) \quad (7)$$

$$Z_e = (T_s - T_e)/\Gamma \quad (8)$$

In eq. 8, α is the planetary albedo and S = 342 W m^{-2}. This approach reproduces the ΔZ_{TP} magnitudes in the GISS-E2.1 simulations when using α = 0.30 for PI and PD, α = 0.32 – 0.33 for the LGM (Trenberth et al., 2009; Köhler et al., 2010; Donohoe & Battisti, 2011; Sherwood et al., 2020). Together with the ΔZ_{O3} estimates outlined above and ΔZ_{SL} = −0.13 km for the LGM (Clark & Mix, 2002), eq. 5 yields a ΔZ_{eff} lowering of several hundred meters for the LGM compared to the PI. Invoking a minor lapse-rate steepening consistent with the model meteorologies (~0.1°C/km) reproduces the 3D-model-based ΔZ_{TP} and ΔZ_{eff} estimates (Table 2). We note that these calculations do not consider the expected warming of the stratosphere at the LGM (Rind et al., 2009; Wang et al., 2020) which would tend to reduce the magnitude of ΔZ_{TP} slightly. However, the magnitude of modeled ΔZ_{TP} values is consistent with previous studies (Noda et al., 2018). These ΔZ_{eff} estimates, from the 3D model and 1D energy balance, suggest that the change in effective mean altitude of isotope exchange at the LGM will yield a warm bias of several degrees Celsius, with a precise magnitude that depends on the assumed change in the global-mean lapse rate.

4.3 Estimating the upper-tropospheric cooling during the LGM. The LGM upper tropospheric cooling ($\Delta T_{10\text{-}11km} > 0$) can be expressed in terms of the Δ_{36} proxy cooling ($\Delta T_{proxy} > 0$), the change in effective altitude for isotope reordering (Section 4.2.4), and the assumed LGM lapse rate:

$$\Delta T_{10\text{-}11km} = \Delta T_{proxy} - \Delta Z_{eff} \times \Gamma \quad (9)$$

Equations 5-9 can thus be used to constrain $\Delta T_{10\text{-}11km}$ at the LGM. Because the LGM lapse rate is not known *a priori*, we evaluate $\Delta T_{10\text{-}11km}$ for Γ = 6.0 – 7.5 °C/km, a plausible range based on previous studies (Loomis et al., 2017). We use the mean SAT of $T_{s,PI}$ = 12.8 ± 0.5 °C from the LGM reanalysis (Tierney & Osman, 2021). To bracket the predictions, we use ΔZ_{O3} of 0 – 0.4 km and ΔT_{proxy} = 3 – 5°C, which reflects range of cold biases expected from the change in E_{trop} and F_{ST} (see above). We note that ΔZ_{O3} = 0 corresponds to ΔT_{proxy} = 5°C, wherein the tropospheric O_3 burden at the LGM is unchanged from the PI; as such, it constitutes the lower limit for ΔZ_{eff} and the upper bound to the $\Delta T_{10\text{-}11km}$ vs. Γ relationship consistent with the Δ_{36} proxy. Conversely, ΔZ_{O3} = 0.4 km corresponds to ΔT_{proxy} = 3°C, the lower bound to the $\Delta T_{10\text{-}11km}$ vs. Γ relationship.

Figure 5 shows the array of $\Delta T_{10\text{-}11km}$ values consistent with the range of clumped-isotope proxy constraints, along with other relevant constraints on the upper-tropospheric cooling. The first ancillary constraint is the mean surface cooling (5.4°C); the positive water vapor feedback (Soden & Held, 2006) implies that the upper-tropospheric cooling must be at least as large as at the surface in the global mean. Similarly, the cooling associated with the moist

adiabatic response in the tropics (11.3 ± 0.9°C cooling at 11 km for a 3.3 ± 0.3°C cooling and a constant 80% relative humidity at the surface) sets a plausible upper limit to $\Delta T_{10\text{-}11km}$. The real upper-tropospheric response in the tropics is likely weaker than for an undiluted moist adiabat, owing to the entrainment of unsaturated air into ascending plumes; however, the near-surface relative humidity may also be slightly lower in cooler climates (Schneider et al., 2010; Tripati et al., 2014), strengthening the response somewhat somewhat. The mean polar surface cooling (10.3°C) corroborates this upper limit to $\Delta T_{10\text{-}11km}$ because increased tropospheric static stability in cold climates leads to a shoaling of extratropical lapse rates (Manabe & Wetherald, 1975; Stone & Carlson, 1979; Schneider et al., 2010): mean upper-tropospheric temperatures will cool less than at the surface in the extratropics. We thus adopt the moist-adiabatic response as a conservative upper limit on $\Delta T_{10\text{-}11km}$, as the shoaling of extratropical lapse rates would reduce the global-mean upper-tropospheric cooling.

The range of lapse rates compatible with the surface temperature change, the Δ_{36} proxy constraint, and the tropical moist adiabatic limit is 6.1 – 7.1°C/km at the LGM, with a mean estimated steepening of –0.2 – 0.4°C/km from the preindustrial value of 6.5°C/km. Thus, the clumped-isotope constraint is consistent with a minor or no change in the global-mean lapse rate at the LGM. The result is robust across the 95% confidence intervals in the LGM reanalysis, the range of planetary albedo estimated for the LGM (0.32 – 0.33), as well as the uncertainty in ΔT_{proxy}. The 3D model results are broadly consistent with this range in LGM upper-tropospheric cooling.

4.4. Comparison to other observational and modeling results. The results of this study suggest that the LGM lapse-rate results from East Africa (0.9°C/km steepening) (Loomis et al., 2017) do not reflect the global-mean response. A highly improbable ΔT_{proxy} cold bias of ~5°C (as opposed to 1°C), driven by a several-fold reduction in tropospheric O_3 burden or increase in STT flux would be required to reconcile our data with the East-African results, if the latter were globally representative. Alternately, a LGM reduction in tropical near-surface relative humidity or increase in entrainment during tropical convection (Tripati et al., 2014) could explain larger lapse-rate changes in the tropics; however, the clumped-isotope data imply that extratropical lapse rate shoaling must temper any tendency toward a large tropical lapse-rate steepening. We note that high-altitude temperatures and terrestrial lapse rates inferred from snowline lowering and pollen assemblages are limited to altitudes 3 – 5 km above sea level, where temperatures can vary regionally due to large-scale circulation. In addition, along-slope lapse rates can be steeper than in free troposphere (Farrera, et al., 1999; Porter, 2000; Kageyama et al., 2005). Consequently, lapse rates obtained from terrestrial archives may simply reflect more localized climatic trends rather than the global tendency.

The lapse-rate climate feedback is the largest negative feedback diagnostic routinely evaluated in climate models (Soden & Held, 2006), so constraining the climate-dependent lapse-rate change using observations may yield insight on potential biases in model physics. Results from the Climate Model Intercomparison Project 5 / PMIP3 predict a LGM lapse-rate steepening of 0.2 – 0.6°C/km (Loomis et al., 2017), which is consistent with that implied by the clumped-isotope constraint. The global-scale inaccuracy of these models therefore appears to be subtle if present. We suggest that the previously documented proxy-model disagreements in the tropics may be related to the representation of local hydroclimate, land-atmosphere feedbacks, or surface topography at specific sites (Baldwin et al., 2021) rather than the planetary-scale energy balance.

5 Conclusions

Our findings demonstrate that clumped isotopes of O_2 in ice cores can provide novel insights into the past climate of the upper troposphere. The broad spatial integration of tropospheric temperatures captured by the Δ_{36} proxy yields a global-scale snapshot of high-altitude climate that is inaccessible through other means. We find quantitative agreement between the simulated and observed changes in tropospheric Δ_{36} value over a range of conditions, the former of which suggests a minor lapse-rate steepening (~0.1°C/km) at the LGM. Yet, the measurement-model agreement found here—particularly for the "high-fire" LGM-DA to PI scenario—does not by itself preclude steeper lapse-rate responses to climate. For example, a smaller LGM reduction in the tropospheric O_3 burden than predicted can offset the effects of lapse-rate steepening in the model, even for the same surface cooling. Nevertheless, energy balance constraints also require a small or negligible global lapse-rate change at the LGM (–0.2 – 0.4°C/km) to be consistent with the Δ_{36} data. While uncertainties about past tropospheric O_3 and stratosphere-troposphere dynamics remain, the climate sensitivity of the tropospheric Δ_{36} value may eventually allow it to provide a new constraint on the phasing of greenhouse-gas concentrations, global temperatures, and changes in atmospheric chemistry. Moreover, when interpreted in the context of surface temperature records, the evolution of high-altitude temperatures may offer insights on the atmospheric heat budget in different climates.

Acknowledgments

This work was supported by the National Science Foundation (grants AGS-2002422 and AGS-2002414) and the David and Lucile Packard Foundation Science & Engineering Fellowship. We thank G. Hargreaves, M. Twickler and R. Nunn at the National Science Foundation Ice Core Facility for ice core sampling assistance and curation. We thank T. Sun for help in the laboratory. The authors declare no conflict of interest.

Open Research

The ice core clumped isotope measured data is available as Supplementary information with this publication and can also be downloaded from https://doi.pangaea.de/10.1594/PANGAEA.940250 and https://doi.pangaea.de/10.1594/PANGAEA.940249. The LGM data assimilation meteorology files can be found at https://doi.org/10.5281/zenodo.5171432. The MATLAB codes for offline computation of Δ_{36} and effective re-ordering altitudes used in this study is available from authors upon reasonable request.

Conflict of Interest Statement

The authors have no conflict of interest to declare.

References

Abe-Ouchi, A., Segawa, T., & Saito, F. (2007). Climatic Conditions for modelling the Northern Hemisphere ice sheets throughout the ice age cycle. *Climate of the Past*, *3*(3), 423–438. https://doi.org/10.5194/cp-3-423-2007

Alexander, B., Savarino, J., Barkov, N. I., Delmas, R. J., & Thiemens, M. H. (2002). Climate driven changes in the oxidation pathways of atmospheric sulfur. *Geophysical Research Letters*, *29*(14), 30-1-30–4. https://doi.org/10.1029/2002GL014879

Anklin, M., Schwander, J., Stauffer, B., Tschumi, J., Fuchs, A., Barnola, J. M., & Raynaud, D. (1997). CO2 record between 40 and 8 kyr B.P. from the Greenland Ice Core Project ice core. *Journal of Geophysical Research: Oceans*, *102*(C12), 26539–26545. https://doi.org/10.1029/97JC00182

Annan, J. D., & Hargreaves, J. C. (2013). A new global reconstruction of temperature changes at the Last Glacial Maximum. *Climate of the Past*, *9*(1), 367–376. https://doi.org/10.5194/cp-9-367-2013

Atkinson, R. (1997). Gas-Phase Tropospheric Chemistry of Volatile Organic Compounds: 1. Alkanes and Alkenes. *Journal of Physical and Chemical Reference Data*, *26*(2), 215. https://doi.org/10.1063/1.556012

Baldwin, J. W., Atwood, A. R., Vecchi, G. A., & Battisti, D. S. (2021). Outsize Influence of Central American Orography on Global Climate. *AGU Advances*, *2*(2), e2020AV000343. https://doi.org/10.1029/2020AV000343

Bony, S., Colman, R., Kattsov, V. M., Allan, R. P., Bretherton, C. S., Dufresne, J. L., et al. (2006, August 1). How well do we understand and evaluate climate change feedback processes? *Journal of Climate*. American Meteorological Society. https://doi.org/10.1175/JCLI3819.1

Bony, S., Stevens, B., Frierson, D. M. W., Jakob, C., Kageyama, M., Pincus, R., et al. (2015). Clouds, circulation and climate sensitivity. *Nature Geoscience*, *8*(4), 261–268. https://doi.org/10.1038/ngeo2398

Braconnot, P., Harrison, S. P., Kageyama, M., Bartlein, P. J., Masson-Delmotte, V., Abe-Ouchi, A., et al. (2012, June 25). Evaluation of climate models using palaeoclimatic data. *Nature Climate Change*. Nature Publishing Group. https://doi.org/10.1038/nclimate1456

Buizert, C., Cuffey, K. M., Severinghaus, J. P., Baggenstos, D., Fudge, T. J., Steig, E. J., et al. (2015). The WAIS Divide deep ice core WD2014 chronology – Part 1: Methane synchronization (68-31 ka BP) and the gas age-ice age difference. *Climate of the Past*, *11*(2), 153–173. https://doi.org/10.5194/cp-11-153-2015

469 Chen, Q., Schmidt, J. A., Shah, V., Jaeglé, L., Sherwen, T., & Alexander, B. (2017). Sulfate production by reactive
470 bromine: Implications for the global sulfur and reactive bromine budgets. *Geophysical Research Letters*,
471 *44*(13), 7069–7078. https://doi.org/10.1002/2017GL073812
472 Clark, P. U., & Mix, A. C. (2002). Ice sheets and sea level of the Last Glacial Maximum. *Quaternary Science*
473 *Reviews*, *21*(1–3), 1–7. https://doi.org/10.1016/S0277-3791(01)00118-4
474 Donohoe, A., & Battisti, D. S. (2011). Atmospheric and Surface Contributions to Planetary Albedo. *Journal of*
475 *Climate*, *24*(16), 4402–4418. https://doi.org/10.1175/2011JCLI3946.1
476 Eastham, S. D., Weisenstein, D. K., & Barrett, S. R. H. (2014). Development and evaluation of the unified
477 tropospheric–stratospheric chemistry extension (UCX) for the global chemistry-transport model GEOS-
478 Chem. *Atmospheric Environment*, *89*, 52–63. https://doi.org/10.1016/J.ATMOSENV.2014.02.001
479 Farrera, I., Harrison, S. P., Prentice, I. C., Ramstein, G., Guiot, J., Bartlein, P. J., Bonnefille, R., Bush, M., Cramer,
480 W., Von Grafenstein, U., et al. (1999). Tropical climates at the Last Glacial Maximum: A new synthesis of
481 terrestrial palaeoclimate data. I. Vegetation, lake-levels and geochemistry. *Climate Dynamics*, *15*(11), 823–
482 856. https://doi.org/10.1007/s003820050317
483 Farrera, I., Harrison, S. P., Prentice, I. C., Ramstein, G., Guiot, J., Bartlein, P. J., Bonnefille, R., Bush, M., Cramer,
484 W., von Grafenstein, U., et al. (1999). Tropical climates at the Last Glacial Maximum: a new synthesis of
485 terrestrial palaeoclimate data. I. Vegetation, lake-levels and geochemistry. *Climate Dynamics*, *15*(11), 823–
486 856. https://doi.org/10.1007/s003820050317
487 Fleurat-Lessard, P., Grebenshchikov, S. Y., Schinke, R., Janssen, C., & Kranskowsky, D. (2003). Isotope
488 dependence of the O+O2 exchange reaction: Experiment and theory. *Journal of Chemical Physics*, *119*(9),
489 4700–4712. https://doi.org/10.1063/1.1595091
490 Fu, Q., Lin, P., Solomon, S., & Hartmann, D. L. (2015). Observational evidence of strengthening of the Brewer-
491 Dobson circulation since 1980. *Journal of Geophysical Research: Atmospheres*, *120*(19), 10214–10228.
492 https://doi.org/10.1002/2015JD023657
493 Fu, Qiang, White, R. H., Wang, M., Alexander, B., Solomon, S., Gettelman, A., et al. (2020). The Brewer-Dobson
494 Circulation During the Last Glacial Maximum. *Geophysical Research Letters*, *47*(5), e2019GL086271.
495 https://doi.org/10.1029/2019GL086271

Geng, L., Murray, L. T., Mickley, L. J., Lin, P., Fu, Q., Schauer, A. J., & Alexander, B. (2017). Isotopic evidence of multiple controls on atmospheric oxidants over climate transitions. *Nature*, *546*(7656), 133–136. https://doi.org/10.1038/nature22340

von Glasow, R., von Kuhlmann, R., Lawrence, M. G., Platt, U., & Crutzen, P. J. (2004). Impact of reactive bromine chemistry in the troposphere. *Atmospheric Chemistry and Physics*, *4*(11/12), 2481–2497. https://doi.org/10.5194/ACP-4-2481-2004

Holton, J. R., Haynes, P. H., McIntyre, M. E., Douglass, A. R., Rood, R. B., & Pfister, L. (1995). Stratosphere-troposphere exchange. *Reviews of Geophysics*, *33*(4), 403. https://doi.org/10.1029/95RG02097

Horowitz, H. M., Jacob, D. J., Zhang, Y., DIbble, T. S., Slemr, F., Amos, H. M., et al. (2017). A new mechanism for atmospheric mercury redox chemistry: Implications for the global mercury budget. *Atmospheric Chemistry and Physics*, *17*(10), 6353–6371. https://doi.org/10.5194/ACP-17-6353-2017

Kageyama, M., Harrison, S. P., & Abe-Ouchi, A. (2005). The depression of tropical snowlines at the last glacial maximum: What can we learn from climate model experiments? *Quaternary International*, *138–139*, 202–219. https://doi.org/10.1016/j.quaint.2005.02.013

Kageyama, M., Albani, S., Braconnot, P., Harrison, S. P., Hopcroft, P. O., Ivanovic, R. F., et al. (2017). The PMIP4 contribution to CMIP6 – Part 4: Scientific objectives and experimental design of the PMIP4-CMIP6 Last Glacial Maximum experiments and PMIP4 sensitivity experiments. *Geoscientific Model Development*, *10*(11), 4035–4055. https://doi.org/10.5194/gmd-10-4035-2017

Kageyama, M., Harrison, S. P., Kapsch, M.-L., Lofverstrom, M., Lora, J. M., Mikolajewicz, U., et al. (2021). The PMIP4 Last Glacial Maximum experiments: preliminary results and comparison with the PMIP3 simulations. *Climate of the Past*, *17*(3), 1065–1089. https://doi.org/10.5194/cp-17-1065-2021

Kaplan, J. O., Folberth, G., & Hauglustaine, D. A. (2006). Role of methane and biogenic volatile organic compound sources in late glacial and Holocene fluctuations of atmospheric methane concentrations. *Global Biogeochemical Cycles*, *20*(2), n/a-n/a. https://doi.org/10.1029/2005GB002590

Kaplan, J. O., Pfeiffer, M., Kolen, J. C. A., & Davis, B. A. S. (2016). Large Scale Anthropogenic Reduction of Forest Cover in Last Glacial Maximum Europe. *PLOS ONE*, *11*(11), e0166726. https://doi.org/10.1371/journal.pone.0166726

Kelley, M., Schmidt, G. A., Nazarenko, L. S., Bauer, S. E., Ruedy, R., Russell, G. L., et al. (2020). GISS-E2.1: Configurations and Climatology. *Journal of Advances in Modeling Earth Systems*, *12*(8), e2019MS002025. https://doi.org/10.1029/2019MS002025

Köhler, P., Bintanja, R., Fischer, H., Joos, F., Knutti, R., Lohmann, G., & Masson-Delmotte, V. (2010). What caused Earth's temperature variations during the last 800,000 years? Data-based evidence on radiative forcing and constraints on climate sensitivity. *Quaternary Science Reviews*, *29*(1), 129–145. https://doi.org/10.1016/j.quascirev.2009.09.026

Loomis, S. E., Russell, J. M., Verschuren, D., Morrill, C., De Cort, G., Sinninghe Damsté, J. S., et al. (2017). The tropical lapse rate steepened during the Last Glacial Maximum. *Science Advances*, *3*(1), e1600815. https://doi.org/10.1126/sciadv.1600815

Loulergue, L., Schilt, A., Spahni, R., Masson-Delmotte, V., Blunier, T., Lemieux, B., et al. (2008). Orbital and millennial-scale features of atmospheric CH4 over the past 800,000 years. *Nature*, *453*(7193), 383–386. https://doi.org/10.1038/nature06950

Manabe, S., & Wetherald, R. T. (1975). The Effects of Doubling the CO2 Concentration on the climate of a General Circulation Model. *Journal of the Atmospheric Sciences*, *32*(1), 3–15.

Martinerie, P., Brasseur, G. P., & Granier, C. (1995). The chemical composition of ancient atmospheres: A model study constrained by ice core data. *Journal of Geophysical Research*, *100*(D7), 14291. https://doi.org/10.1029/95JD00826

Monnin, E., Indermühle, A., Dällenbach, A., Flückiger, J., Stauffer, B., Stocker, T. F., et al. (2001). Atmospheric CO2 concentrations over the last glacial termination. *Science*, *291*(5501), 112–114. https://doi.org/10.1126/science.291.5501.112

Murray, L. T., Mickley, L. J., Kaplan, J. O., Sofen, E. D., Pfeiffer, M., & Alexander, B. (2014). Factors controlling variability in the oxidative capacity of the troposphere since the Last Glacial Maximum. *Atmospheric Chemistry and Physics*, *14*(7), 3589–3622. https://doi.org/10.5194/acp-14-3589-2014

Murray, Lee T., Leibensperger, E. M., Orbe, C., Mickley, L. J., & Sulprizio, M. (2021). GCAP 2.0: a global 3-D chemical-transport model framework for past, present, and future climate scenarios. *Geoscientific Model Development*, *14*(9), 5789–5823. https://doi.org/10.5194/GMD-14-5789-2021

Neu, J. L., Flury, T., Manney, G. L., Santee, M. L., Livesey, N. J., & Worden, J. (2014). Tropospheric ozone variations governed by changes in stratospheric circulation. *Nature Geoscience 2014 7:5*, *7*(5), 340–344. https://doi.org/10.1038/ngeo2138

Noda, S., Kodera, K., Adachi, Y., Deushi, M., Kitoh, A., Mizuta, R., et al. (2018). Mitigation of Global Cooling by Stratospheric Chemistry Feedbacks in a Simulation of the Last Glacial Maximum. *Journal of Geophysical Research: Atmospheres*, *123*(17), 9378–9390. https://doi.org/10.1029/2017JD028017

Osman, M. B., Tierney, J. E., Zhu, J., Tardif, R., Hakim, G. J., King, J., & Poulsen, C. J. (2021). Globally resolved surface temperatures since the Last Glacial Maximum. *Nature*.

Osthoff, H. D., Roberts, J. M., Ravishankara, A. R., Williams, E. J., Lerner, B. M., Sommariva, R., et al. (2008). High levels of nitryl chloride in the polluted subtropical marine boundary layer. *Nature Geoscience 2008 1:5*, *1*(5), 324–328. https://doi.org/10.1038/ngeo177

Otto-Bliesner, B. L., Brady, E. C., Clauzet, G., Tomas, R., Levis, S., & Kothavala, Z. (2006). Last glacial maximum and Holocene climate in CCSM3. *Journal of Climate*, *19*(11), 2526–2544. https://doi.org/10.1175/JCLI3748.1

Parrenin, F., Masson-Delmotte, V., Köhler, P., Raynaud, D., Paillard, D., Schwander, J., et al. (2013). Synchronous change of atmospheric CO2and antarctic temperature during the last deglacial warming. *Science*, *339*(6123), 1060–1063. https://doi.org/10.1126/science.1226368

Pfeiffer, M., Spessa, A., & Kaplan, J. O. (2013). A model for global biomass burning in preindustrial time: LPJ-LMfire (v1.0). *Geoscientific Model Development*, *6*(3), 643–685. https://doi.org/10.5194/gmd-6-643-2013

Porter, S. C. (2000). Snowline depression in the tropics during the last glaciation. *Quaternary Science Reviews*, *20*(10), 1067–1091. https://doi.org/10.1016/S0277-3791(00)00178-5

Rasmussen, S. O., Bigler, M., Blockley, S. P., Blunier, T., Buchardt, S. L., Clausen, H. B., et al. (2014). A stratigraphic framework for abrupt climatic changes during the Last Glacial period based on three synchronized Greenland ice-core records: refining and extending the INTIMATE event stratigraphy. *Quaternary Science Reviews*, *106*, 14–28. https://doi.org/10.1016/j.quascirev.2014.09.007

Rind, D., Suozzo, R., Balachandran, N. K., Lacis, A., & Russell, G. (1988). The GISS Global Climate-Middle Atmosphere Model. Part I: Model Structure and Climatology. *Journal of the Atmospheric Sciences*, *45*(3), 329–370. https://doi.org/10.1175/1520-0469(1988)045<0329:TGGCMA>2.0.CO;2

578 Rind, D., Chandler, M., Lonergan, P., & Lerner, J. (2001). Climate change and the middle atmosphere: 5.
579 Paleostratosphere in cold and warm climates. *Journal of Geophysical Research: Atmospheres*, *106*(D17),
580 20195–20212. https://doi.org/10.1029/2000JD900548
581 Rind, D., Lerner, J., McLinden, C., & Perlwitz, J. (2009). Stratospheric ozone during the Last Glacial Maximum.
582 *Geophysical Research Letters*, *36*(9), L09712. https://doi.org/10.1029/2009GL037617
583 Roberts, J. M., Osthoff, H. D., Brown, S. S., & Ravishankara, A. R. (2008). N2O5 Oxidizes Chloride to Cl2 in
584 Acidic Atmospheric Aerosol. *Science*, *321*(5892), 1059. https://doi.org/10.1126/SCIENCE.1158777
585 Saiz-Lopez, A., & Glasow, R. von. (2012). Reactive halogen chemistry in the troposphere. *Chemical Society*
586 *Reviews*, *41*(19), 6448–6472. https://doi.org/10.1039/C2CS35208G
587 Schmidt, G. A., Ruedy, R., Hansen, J. E., Aleinov, I., Bell, N., Bauer, M., et al. (2006). Present-Day Atmospheric
588 Simulations Using GISS ModelE: Comparison to In Situ, Satellite, and Reanalysis Data. *Journal of*
589 *Climate*, *19*(2), 153–192. https://doi.org/10.1175/JCLI3612.1
590 Schmidt, J. A., Jacob, D. J., Horowitz, H. M., Hu, L., Sherwen, T., Evans, M. J., et al. (2016). Modeling the
591 observed tropospheric BrO background: Importance of multiphase chemistry and implications for ozone,
592 OH, and mercury. *Journal of Geophysical Research: Atmospheres*, *121*(19), 11,819-11,835.
593 https://doi.org/10.1002/2015JD024229
594 Schmittner, A., Urban, N. M., Shakun, J. D., Mahowald, N. M., Clark, P. U., Bartlein, P. J., et al. (2011). Climate
595 sensitivity estimated from temperature reconstructions of the Last Glacial Maximum. *Science*, *334*(6061),
596 1385–1388. https://doi.org/10.1126/science.1203513
597 Schneider, T., O'Gorman, P. A., & Levine, X. J. (2010). WATER VAPOR AND THE DYNAMICS OF CLIMATE
598 CHANGES. *Reviews of Geophysics*, *48*(3), 3001. https://doi.org/10.1029/2009RG000302
599 Seierstad, I. K., Abbott, P. M., Bigler, M., Blunier, T., Bourne, A. J., Brook, E., et al. (2014). Consistently dated
600 records from the Greenland GRIP, GISP2 and NGRIP ice cores for the past 104ka reveal regional
601 millennial-scale δ18O gradients with possible Heinrich event imprint. *Quaternary Science Reviews*, *106*,
602 29–46. https://doi.org/10.1016/j.quascirev.2014.10.032
603 Seltzer, A. M., Ng, J., Aeschbach, W., Kipfer, R., Kulongoski, J. T., Severinghaus, J. P., & Stute, M. (2021).
604 Widespread six degrees Celsius cooling on land during the Last Glacial Maximum. *Nature*, *593*(7858),
605 228–232. https://doi.org/10.1038/s41586-021-03467-6

606 Severinghaus, J. P. (2015). Low-res d15N and d18O of O2 in the WAIS Divide 06A Deep Core [Data set]. U.S.
607 Antarctic Program Data Center (USAP-DC), via National Snow and Ice Data Center (NSIDC).
608 https://doi.org/10.7265/N5S46PWD
609 Severinghaus, J. P., Grachev, A., Luz, B., & Caillon, N. (2003). A method for precise measurement of argon 40/36
610 and krypton/argon ratios in trapped air in polar ice with applications to past firn thickness and abrupt
611 climate change in Greenland and at Siple Dome, Antarctica. *Geochimica et Cosmochimica Acta*, *67*(3),
612 325–343. https://doi.org/10.1016/S0016-7037(02)00965-1
613 Severinghaus, J. P., Beaudette, R., Headly, M. A., Taylor, K., & Brook, E. J. (2009). Oxygen-18 of O2 Records the
614 Impact of Abrupt Climate Change on the Terrestrial Biosphere. *Science*.
615 https://doi.org/10.1126/science.1169473
616 Shepherd, T. G. (2014). Atmospheric circulation as a source of uncertainty in climate change projections. *Nature*
617 *Geoscience*, *7*(10), 703–708. https://doi.org/10.1038/ngeo2253
618 Sherwen, T., Evans, M. J., Carpenter, L. J., Andrews, S. J., Lidster, R. T., Dix, B., et al. (2016). Iodine's impact on
619 tropospheric oxidants: A global model study in GEOS-Chem. *Atmospheric Chemistry and Physics*, *16*(2),
620 1161–1186. https://doi.org/10.5194/acp-16-1161-2016
621 Sherwen, Tomás, Schmidt, J. A., Evans, M. J., Carpenter, L. J., Großmann, K., Eastham, S. D., et al. (2016). Global
622 impacts of tropospheric halogens (Cl, Br, I) on oxidants and composition in GEOS-Chem. *Atmospheric*
623 *Chemistry and Physics*, *16*(18), 12239–12271. https://doi.org/10.5194/acp-16-12239-2016
624 Sherwood, S. C., Webb, M. J., Annan, J. D., Armour, K. C., Forster, P. M., Hargreaves, J. C., et al. (2020). An
625 Assessment of Earth's Climate Sensitivity Using Multiple Lines of Evidence. *Reviews of Geophysics*,
626 *58*(4), e2019RG000678. https://doi.org/10.1029/2019RG000678
627 Sherwood, Steven C., Bony, S., & Dufresne, J.-L. (2014). Spread in model climate sensitivity traced to atmospheric
628 convective mixing. *Nature*, *505*(7481), 37–42. https://doi.org/10.1038/nature12829
629 Sigl, M., Fudge, T. J., Winstrup, M., Cole-Dai, J., Ferris, D., McConnell, J. R., et al. (2016). The WAIS Divide deep
630 ice core WD2014 chronology – Part 2: Annual-layer counting (0–31 ka BP). *Climate of the Past*, *12*(3),
631 769–786. https://doi.org/10.5194/cp-12-769-2016
632 Soden, B. J., & Held, I. M. (2006). An assessment of climate feedbacks in coupled ocean-atmosphere models.
633 *Journal of Climate*, *19*(14), 3354–3360. https://doi.org/10.1175/JCLI3799.1

634 Spahni, R., Chappellaz, J., Stocker, T. F., Loulergue, L., Hausammann, G., Kawamura, K., et al. (2005).
635 Atmospheric science: Atmospheric methane and nitrous oxide of the late pleistocene from Antarctic Ice
636 Cores. *Science*, *310*(5752), 1317–1321. https://doi.org/10.1126/science.1120132
637 Stansell, N. D., Polissar, P. J., & Abbott, M. B. (2007). Last glacial maximum equilibrium-line altitude and paleo-
638 temperature reconstructions for the Cordillera de Mérida, Venezuelan Andes. *Quaternary Research*, *67*(1),
639 115–127. https://doi.org/10.1016/j.yqres.2006.07.005
640 Stone, P. H., & Carlson, J. H. (1979). Atmospheric Lapse Rate Regimes and Their Parameterization. *Journal of the*
641 *Atmospheric Sciences*, *36*(3), 415–423.
642 Thompson, A. M., Chappellaz, J. A., Fung, I. Y., & Kucsera, T. L. (1993). The atmospheric CH4 increase since the
643 Last Glacial Maximum: (2). Interactions with oxidants. *Tellus B*, *45*(3), 242–257.
644 https://doi.org/10.1034/j.1600-0889.1993.t01-2-00003.x
645 Thompson, L. G., Mosley-Thompson, E., Davis, M. E., Lin, P.-N., Henderson, K. A., Cole-Dai, J., et al. (1995).
646 Late Glacial Stage and Holocene Tropical Ice Core Records from Huascarán, Peru. *Science*.
647 https://doi.org/10.1126/science.269.5220.46
648 Thompson, L. G., Davis, M. E., Mosley-Thompson, E., Sowers, T. A., Henderson, K. A., Zagorodnov, V. S., et al.
649 (1998). A 25,000-Year Tropical Climate History from Bolivian Ice Cores. *Science*. Retrieved from
650 https://www.science.org/doi/abs/10.1126/science.282.5395.1858
651 Thompson, Lonnie G. (2000). Ice core evidence for climate change in the Tropics: implications for our future.
652 *Quaternary Science Reviews*, *19*(1), 19–35. https://doi.org/10.1016/S0277-3791(99)00052-9
653 Thompson, Lonnie G., Mosley-Thompson, E., Davis, M. E., Lin, P.-N., Henderson, K., & Mashiotta, T. A. (2003).
654 Tropical Glacier and Ice Core Evidence of Climate Change on Annual to Millennial Time Scales. In H. F.
655 Diaz (Ed.), *Climate Variability and Change in High Elevation Regions: Past, Present & Future* (pp. 137–
656 155). Dordrecht: Springer Netherlands. https://doi.org/10.1007/978-94-015-1252-7_8
657 Thuburn, J., & Craig, G. C. (2000). Stratospheric Influence on Tropopause Height: The Radiative Constraint.
658 *Journal of the Atmospheric Sciences*, *57*(1), 17–28. https://doi.org/10.1175/1520-
659 0469(2000)057<0017:SIOTHT>2.0.CO;2
660 Tierney, J., & Osman, M. (2021). jesstierney/lgmDA: v2.0. https://doi.org/10.5281/ZENODO.5171436

661 Tierney, J. E., Zhu, J., King, J., Malevich, S. B., Hakim, G. J., & Poulsen, C. J. (2020). Glacial cooling and climate
662 sensitivity revisited. *Nature*, *584*(7822), 569–573. https://doi.org/10.1038/s41586-020-2617-x
663 Trenberth, K. E., Fasullo, J. T., & Kiehl, J. (2009). Earth's Global Energy Budget. *Bulletin of the American*
664 *Meteorological Society*, *90*(3), 311–324. https://doi.org/10.1175/2008BAMS2634.1
665 Tripati, A. K., Sahany, S., Pittman, D., Eagle, R. A., Neelin, J. D., Mitchell, J. L., & Beaufort, L. (2014). Modern
666 and glacial tropical snowlines controlled by sea surface temperature and atmospheric mixing. *Nature*
667 *Geoscience*, *7*(3), 205–209. https://doi.org/10.1038/ngeo2082
668 Valdes, P. J. (2005). The ice age methane budget. *Geophysical Research Letters*, *32*(2), L02704.
669 https://doi.org/10.1029/2004GL021004
670 Wang, M., Fu, Q., Solomon, S., White, R. H., & Alexander, B. (2020). Stratospheric Ozone in the Last Glacial
671 Maximum. *Journal of Geophysical Research: Atmospheres*, *125*(21).
672 https://doi.org/10.1029/2020JD032929
673 Wang, X., Jacob, D. J., Eastham, S. D., Sulprizio, M. P., Zhu, L., Chen, Q., et al. (2019). The role of chlorine in
674 global tropospheric chemistry. *Atmospheric Chemistry and Physics*, *19*(6), 3981–4003.
675 https://doi.org/10.5194/ACP-19-3981-2019
676 Wang, X., Jacob, D. J., Downs, W., Zhai, S., Zhu, L., Shah, V., et al. (2021). Global tropospheric halogen (Cl, Br, I)
677 chemistry and its impact on oxidants. *Atmospheric Chemistry and Physics*, *21*(18), 13973–13996.
678 https://doi.org/10.5194/ACP-21-13973-2021
679 Wang, Z., Schauble, E. A., & Eiler, J. M. (2004). Equilibrium thermodynamics of multiply substituted isotopologues
680 of molecular gases. *Geochimica et Cosmochimica Acta*, *68*(23), 4779–4797.
681 https://doi.org/10.1016/j.gca.2004.05.039
682 Yang, X., Cox, R. A., Warwick, N. J., Pyle, J. A., Carver, G. D., O'Connor, F. M., & Savage, N. H. (2005).
683 Tropospheric bromine chemistry and its impacts on ozone: A model study. *Journal of Geophysical*
684 *Research: Atmospheres*, *110*(D23), 1–18. https://doi.org/10.1029/2005JD006244
685 Yeung, L. Y., Young, E. D., & Schauble, E. A. (2012). Measurements of 18O18O and 17O 18O in the atmosphere
686 and the role of isotope-exchange reactions. *Journal of Geophysical Research Atmospheres*.
687 https://doi.org/10.1029/2012JD017992

688 Yeung, L. Y., Ash, J. L., & Young, E. D. (2014). Rapid photochemical equilibration of isotope bond ordering in O2.
689 *Journal of Geophysical Research*. https://doi.org/10.1002/2014JD021909
690 Yeung, L. Y., Murray, L. T., Ash, J. L., Young, E. D., Boering, K. A., Atlas, E. L., et al. (2016). Isotopic ordering in
691 atmospheric O2 as a tracer of ozone photochemistry and the tropical atmosphere. *Journal of Geophysical*
692 *Research*. https://doi.org/10.1002/2016JD025455
693 Yeung, L. Y., Murray, L. T., Martinerie, P., Witrant, E., Hu, H., Banerjee, A., et al. (2019). Isotopic constraint on
694 the twentieth-century increase in tropospheric ozone. *Nature*. https://doi.org/10.1038/s41586-019-1277-1
695 Yeung, L. Y., Murray, L. T., Banerjee, A., Tie, X., Yan, Y., Atlas, E. L., et al. (2021). Effects of Ozone
696 Isotopologue Formation on the Clumped-Isotope Composition of Atmospheric O2. *Journal of Geophysical*
697 *Research: Atmospheres*, *126*(14), e2021JD034770. https://doi.org/10.1029/2021JD034770
698
699

700 **Figures and Tables**
701

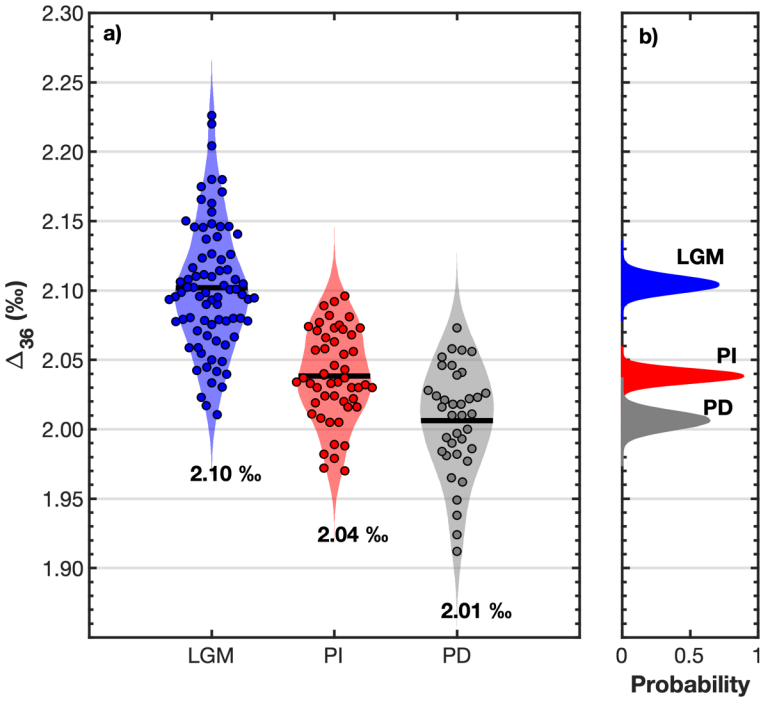

702
703
704 **Figure 1. Comparison of atmospheric Δ_{36} values for the LGM, PI, and PD.** (a) Measured distribution for the
705 LGM (blue), PI (red) & PD (grey). The PI and PD data are from (Yeung et al., 2019). Black lines represent the mean
706 values for each time period, which are shown below each dataset. (b) Kernel-smoothed bootstrap probability density
707 distributions of mean atmospheric Δ_{36} values for the LGM, PI and PD.
708

709

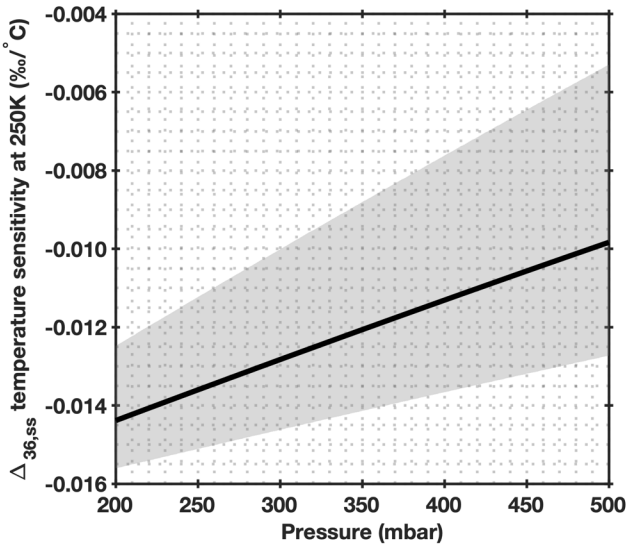

710
711
712 **Figure 2. Sensitivity of endmember Δ_{36} values at photochemical steady state (i.e., $\Delta_{36,ss}$).** Pressures ranging from
713 250 – 450 mbar are comparable to those sampled in the troposphere by the Δ_{36} tracer. The shaded area shows the 2σ
714 uncertainty limits based on the laboratory uncertainty in isotope-exchange rate coefficients (Fleurat-Lessard et al.,
715 2003).
716

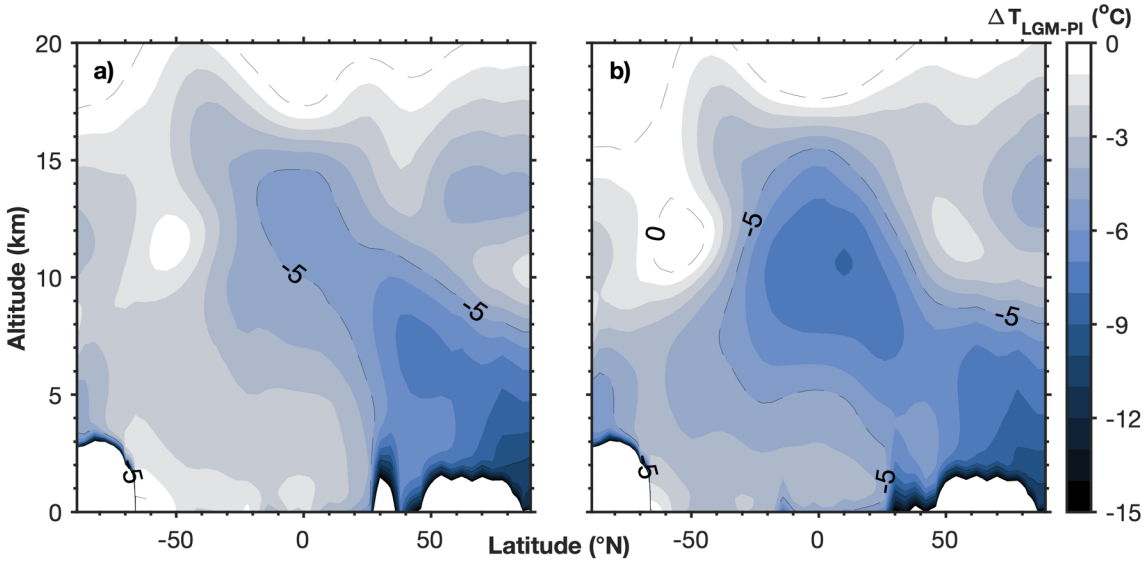

Figure 3. **Zonal-mean air temperature change (LGM relative to PI) using the (a) LGM-GISS and (b) LGM-DA meteorologies**. White spaces at near surface elevation represent modeled changes in elevation during the LGM due to change in ice sheet elevation.

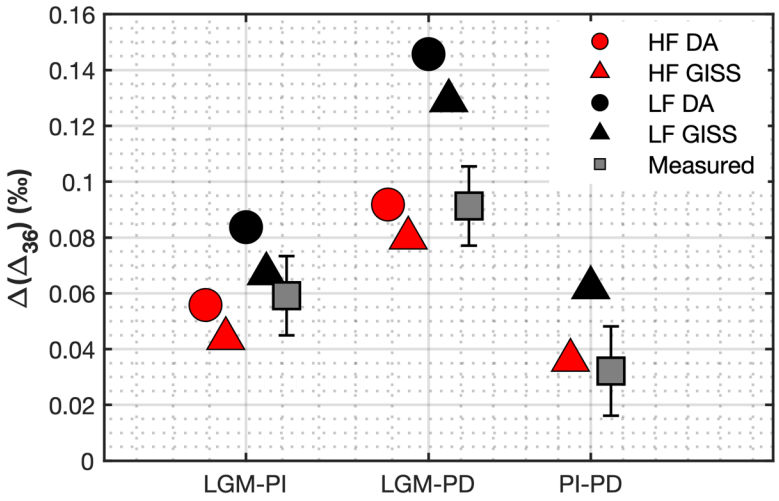

Figure 4: Measured and modeled mean Δ_{36} differences between the LGM, PI and PD. Error bars represent the bootstrap 95% confidence interval.

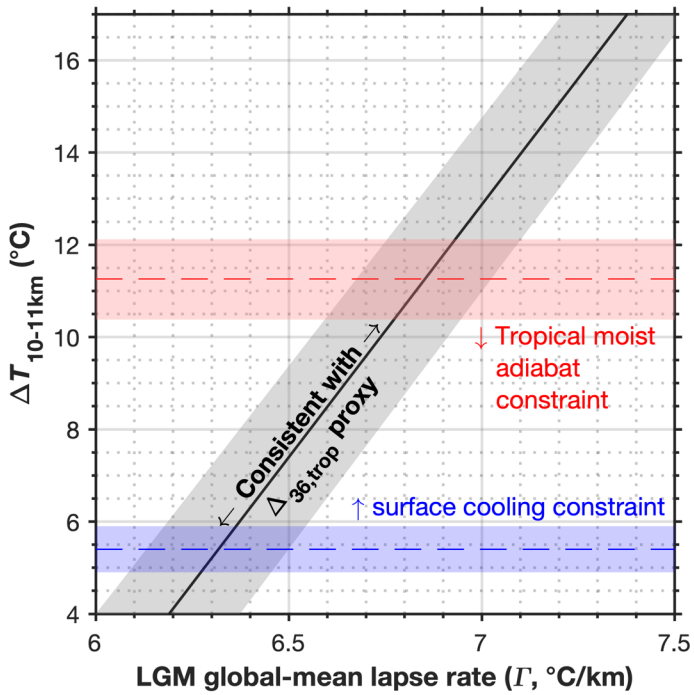

Figure 5. Upper-tropospheric cooling at the LGM compatible with Δ_{36} proxy and thermodynamic, radiative, and dynamical constraints. The shaded areas reflect a conservative range in uncertainty that includes uncertainties in global-mean surface temperature and planetary albedo changes.

731 **Table 1. O_3 burden and Δ_{36} diagnostics derived from model simulations for different climate and biomass-**
732 **burning scenarios.**

Scenario	O_3 burden (Tg O_3)	$\Delta_{36,trop}$ (‰)*	$\Delta_{36,t}$ (‰)†	$\Delta_{36,strat}$ (‰)‡	Mean effective altitude for $\Delta_{36,t}$ (km)§	E_{trop} (10^{19} mol O_2 yr^{-1})	F_{ST} (10^{19} mol O_2 yr^{-1})
LGM-GISS low-fire	239	2.19	2.11	2.51	11.3	1.16	0.28
LGM-GISS high-fire	282	2.14	2.05	2.51	10.9	1.34	0.29
LGM-DA low fire	224	2.20	2.11	2.50	11.3	1.09	0.31
LGM-DA high fire	273	2.15	2.06	2.50	10.9	1.29	0.33
PI low-fire	272	2.12	2.05	2.47	11.6	1.39	0.25
PI high-fire	298	2.09	2.03	2.47	11.4	1.50	0.26
PD	340	2.06	1.99	2.47	11.3	1.73	0.25

733 *Global-mean surface Δ_{36} value
734 †Endmember Δ_{36} value for isotope exchange occurring only in the troposphere
735 ‡Endmember Δ_{36} value for isotope exchange occurring only in the stratosphere
736 §Relative to PI sea level
737

738 **Table 2. Comparison of 3D- and 1D-model -derived ΔZ_{eff} according to eqs. 5 – 8 for a range of low-fire (LF)**
739 **and high-fire (HF) scenarios.**

	ΔZ_{O3}		ΔZ_{TP}		ΔZ_{SL}	ΔZ_{eff}		
	3D	*1D*	*3D*	*1D*		*3D*	*1D*	*Difference*
LGM-GISS – PI LF	0.25	0.27	–0.46	–0.53*	–0.13	–0.34	–0.39	0.05
LGM-GISS – PI HF	0.09	0.11	–0.46	–0.53*	–0.13	–0.50	–0.54	0.04
LGM-DA – PI HF	0.51	0.40	–0.72	–0.68*	–0.13	–0.34	–0.40	0.06
LGM-DA – PI HF	0.30	0.18	–0.72	–0.68*	–0.13	–0.55	–0.63	0.08
PI LF – PD	0.42	0.45	–0.15	–0.11	0.00	–0.28	–0.34	–0.06
PI HF – PD	0.23	0.29	–0.15	–0.11	0.00	–0.08	–0.18	–0.10

740 *For LGM lapse-rate steepening of 0.1°C/km.
741
742